 CMES, vol.72, no.4, pp.337-366, 2011

Calculation of a Deformable Membrane Airfoil in Hovering Flight

D.M.S. Albuquerque[1], **J.M.C. Pereira** [1] **and J.C.F. Pereira**[1,2]

Abstract: A numerical study of fluid-structure interaction is presented for the analysis of viscous flow over a resonant membrane airfoil in hovering flight. A flexible membrane moving with a prescribed stroke period was naturally excited to enter into 1^{st}, 2^{nd} and 3^{rd} mode of vibration according to the selected membrane tension. The Navier-Stokes equations were discretized on a moving body unstructured grid using the finite volume method. The instantaneous membrane position was predicted by the 1D unsteady membrane equation with input from the acting fluid flow forces. Following initial validation against reported rigid airfoils predictions, the model is applied to the dragonfly hovering case for a flapping membrane, pinned at both ends, at a Reynolds number based on the chord length of 157 and 1570. For a prescribed membrane tension corresponding to the first resonance mode, the membrane adopts a stable equilibrium shape that reduces both drag and lift forces relatively to the rigid airfoil values. For higher vibration resonant modes a weak interaction was predicted between the coherent membrane inflated shape and the resulting unsteady wake. For these cases the leading and trailing edges vortices dominate over the membrane shape fluid interaction. Most of the airfoil flexion occurs not from the aero-elastic interactions between the airfoil and the fluid but from the inertial bending of the airfoil on account of its density and tension.

Keywords: unsteady aerodynamics, insect flight, computational fluid dynamics, vortex dynamics, fluid-structure interaction, membrane dynamics.

1 Introduction

Recently interest has grown in developing insect-inspired, low Reynolds number and low aspect ratio (LAR) flapping wings to power Micro Aerial Vehicles (MAVs) to be used in wide-ranging monitoring and surveillance activities, ([e.g. Ellington

[1] Instituto Superior Técnico, Technical University of Lisbon, Av. Rovisco Pais, 1, 1049-001, Lisbon, Portugal.
[2] email:jcfpereira@ist.utl.pt

(1999); Shyy, Berg, and Ljungqvist (1999); Rozhdestvensky and Ryzhov (2003)]. The majority of MAV applications require great manoeuvrability and the ability to hover, consequently there is a growing interest on all aspects of flapping wing operation including wing stiffness and morphing capabilities or even designs going beyond the biological model of inspiration, [e.g. Michelson and Naqvi (2003)].

Nowadays, the unsteady aerodynamics of periodic flapping flight is well known and many theoretical models and experimental studies exist that explain the high lift aerodynamic mechanisms: i) clap and fling see e.g. [Weis-Fogh (1972); Lehmann, Sane, and Dickinson (2005)], ii) leading edge vortex (LEV) or delayed stall [Dickinson and Götz (1993); Ellington, Berg, Willmott, and Thomas (1996); Birch and Dickinson (2001)], iii) wake capturing [Lehmann and Dickinson (1997); Dickinson, Lehmann, and Sane (1999)] and iv) rotational circulation [Lehmann and Dickinson (1997)]. Each mechanism depends on the Reynolds and Strouhal numbers associated with forward or hovering flight [e.g. Andro and Jacquin (2009)]. The force required for uniform or accelerated flight conditions is achieved by changes in the kinematic parameters, such as stroke plane angle, deviation from stroke plane, wing beat amplitude, angular velocity of the wing, etc. In addition to complex kinematics, birds and insects change their camber significantly to achieve the desired flight conditions (see for example the reviews of [Sane (2003); Shyy, Lian, Tang, Viieru, and Liu (2008); Wang (2005)]).

The flapping flight of insects and birds is accompanied by significant bending of flexible wings that have the potential for morphing and to alleviate the effects of gust wind compared with rigid wings [e.g. Smith and Shyy (1995); Shyy, Jenkins, and Smith (1997); Shyy, Berg, and Ljungqvist (1999); Ellington (1999); Thomas and Stancey (2002); Ho, Nassef, Pornsinsirirak, Tai, and Ho (2003); Hu, Tamai, and Murphy (2008); Heathcote, Wang, and Gursul (2008)]. In addition, flexibility may delay the stall and acts as a potential passive flow control method in nature and engineering applications [Rojratsirikul, Wang, and Gursul (2009)]. For this purpose the leading edges should remain rigid to avoid loss of vortex lift by disruption of the unsteady leading edge vortex [e.g. Lisa, Deborah, and Chris (2008); Ho, Nassef, Pornsinsirirak, Tai, and Ho (2003)]. Mammalian flyers such as bats can exhibit extraordinary fight agility and maneuverability in part by the utilization of LAR thin compliant wings as the lifting surface [Galvao, Israeli, Song, Tian, K., Sharon, and B. (2006)].

As is well known aeroelasticity describes the interaction between aerodynamic loads, elastic and inertial forces [Bisplinghoff, Ashley, and Halfman (1996)]. The triangle formed with these three forces illustrates the location of each aeroelastic phenomenon on the diagram according to its relation to the three vertices. Consequently wing bending and flutter, buffeting and dynamic response related with

aircraft design are inside the triangle and involve the three forces coupling. Insects or light MAVs present an higher wing flexibility compared with rigid wings and it is relevant to understand if full 3D viscous fluid-structure interaction is required [Liu (2009)] or it is possible the incorporation of wing flexion into current models [Ansari, Zbikowski, and Knowles (2006)].

Motivation for the present work arises from several wing flexibility studies that indicated the relatively minor role which pressure stresses play in determining the wing shape, (for certain combinations of wing structure and motions). The wing deflexion was not attributed to the aero-elastic interactions between the wing and the fluid but simply to the inertial bending of the wing [e.g. Combes and Daniel (2001); Daniel and Combes (2001); Thomas and Stancey (2002); Kamakoti and Shyy (2002);Sane (2003); Yamada and Yoshimura (2008); Vanella, Fitzgerald, Preidikman, Balaras, and Balachandran (2009)]. Different authors have applied optimization algorithms to increase the performance of rigid airfoils by changing their shape see e.g. [Srinath and Manek (2009); Levin and Shyy (2001)].

The main objective of this work is to investigate to what extent elastic and pressure forces are coupled and modify the surface shape of flapping wings under resonance. We have selected extreme conditions which constitute a class of problems involving the dynamics of shape-changing bodies under resonance in fluids. In other words, does the combined structural and fluid dynamic loads bring the membrane and flow into equilibrium? or alternatively , does it result a non-steady behavior composed of many superimposed structural modes interacting with a highly unsteady wake?

In the present study a linear membrane model is used to compute the deformation with applied aerodynamic loads. The aeroelastic response of an initially flat membrane wing is dominated by pretension in the limit of vanishing material stiffness. We consider a simple two dimensional airfoil in dragonfly hovering, where the lack of forward velocity requires a substantial energy input. For a comprehensive review of the literature see [e.g. Ellington (1984); Van den Berg and Ellington (1997); Wang (2000); Wang (2004); Wang (2005); Thomas, Taylor, Srygley, Nudds, and Bomphrey (2002); Young, Lai, and Germain (2008)].

The phenomenon of resonance in the framework of flapping wings has been only considered relatively to the insect thorax-wings system and related with the very high wing beat frequency that implements mechanical resonance in the thorax to minimize energy expenditure. The flight system of insects is a damped resonator (e.g. Greenewalt (1960); Dudley (2000)) and in the framework of MAV, several flying micromechanisms have been proposed [Isogai, Kamisawa, and Sato (2007)].

The viscous flow patterns and aerodynamic parameters resulting from a flapping flexible membrane operating in resonance mode are, to the authors knowledge, not

been reported. The present work simulates the 1^{st}, 2^{nd} and 3^{rd} vibration modes of a 1D flapping membrane over twenty stroke periods. Comparisons with a rigid airfoil are made for reference purposes. Interest is focused on the membrane deformation and the nature of the unsteady vortex interaction behavior around the flexible-membrane airfoil in resonance mode as well as their effects on the overall aerodynamic performance.

Nowadays, there is a wide offer of numerical techniques that have been successfully applied to flapping wings, among them the method of artificial compressibility [Liu, Ellington, Kawachi, Van den Berg, and Willmott (1998)], the finite element method [Ramamurti and Sandberg (2002)], vortex method [Eldredge (2005)], the immersed boundary-lattice Boltzmann method [Gao and Lu (2008)] and the boundary element method [La Mantia and Dabnichki (2008)]. A computational fluid dynamic (CFD) modeling approach is used to study the unsteady aerodynamics of the flapping airfoil in dragonfly hovering. Although the present study is two-dimensional it was reported that 2D unsteady forces predictions turn out not to be very far away from of 3D experiments [Wang, Birch, and Dickinson (2004)], 2D unsteady simulations have also been used to study the influence of ground effect in hovering flight performance [Gao and Lu (2008)] and [Pereira, Maia, and Pereira (2009)].

In this work, we focus on a hovering flapping flat plate at $Re = 157$ and $Re = 1570$ based upon maximum translational speed and wing chord. At this Reynolds number, turbulence is absent and the issues of numerical resolution can be addressed satisfactorily with a grid moving technique that maintains grid quality over time. Suitable distribution of around 400 thousands computational cells was required to capture the relevant detail of this 2D unsteady flow.

The next section explains the numerical method used for both fluid and membrane models and in particular the mesh used and the efficient moving mesh procedure. This is followed by the validation exercise in which different rigid airfoils predictions in dragonfly mode are compared with reference data. The fourth section presents the results obtained with the flexible membrane airfoil under different modes of vibration. The results section ends with and energetic analysis of the rigid and flexible airfoils by splitting the power required for the motion in pitching and translation motions. The paper ends with summary conclusions.

2 Computational Models for Coupled Fluid-Structure Interaction

2.1 Mathematical model and numerical method for fluid equations

We assume that the fluid is newtonian and incompressible and the Navier-Stokes model for an unsteady flow reads as:

$$\nabla \cdot \mathbf{u} = 0, \tag{1}$$

$$\frac{\partial \mathbf{u}}{\partial t} + (\mathbf{u} \cdot \nabla)\mathbf{u} = -\frac{\nabla p}{\rho} + \nu \nabla^2 \mathbf{u}, \tag{2}$$

We are interested in studying the membrane wing shape changes under elastic and fluid forces and the shape variation effects on the surrounding fluid flow. Due to this coupling it is required to accurately capture the transient behavior of fluid flow and membrane dynamics. The STAR-CD software embodies a numerical finite volume solver, for fluid flow predictions we have selected this software package because of the unstructured grid capabilities with local refinement and non-conformal grid with arbitrary interfaces. The solution of the linear system of equations is obtain by bi-conjugate gradient method with algebraic multigrid preconditioning and PISO (Pressure-Implicit Split-Operator) method is generally very efficient for transient flow computation [Issa (1985)], while the spatial discretization uses a 2^{nd} order convection discretization scheme with a TVD (Total Variation Diminishing) limiter.

2.2 Moving Grid Technique

The moving grid technique is employed to adjust the grid dynamically along with the wing motion and the geometry updates. A non-uniform mesh was used and a high density of nodes is located close to the airfoil and in regions with expected high velocity gradients. Fig. 1 shows the mesh with the computational domain divided in three regions. The sliding interface was located far away from the airfoil, between zone 2 and 3, to reduce the numerical dissipation produced by the interpolation between the moving and steady meshes.

Near the airfoil, at zone one, the mesh extended up to 5 chords and different meshes were generated for each airfoil type used; elliptic, plate and diamond. The second block is delimited by the previous circle and the interface zone, which is extended up to twenty chords from the airfoil. The third zone is defined between the interface zone and the domain's outer border.

A transformation is applied to the zones one and two, similar to a rotor and a stator of a turbomachine, to account for the pitch motion of the airfoil. This is achieved, by imposing in the interface zone a continuity condition, which interpolates information between the steady and the moving meshes.

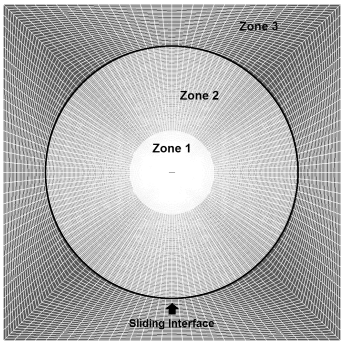

Figure 1: Model's domain and mesh with the 3 zones

The airfoil translational motion is achieved by stretching the zone two. This type of transformation was not applied to zone one to avoid numerical dissipation. The mesh in zone one suffers a translational motion to account for the membrane deformation and the cells in zone three remain unchanged.

In the outer border the slip condition is imposed, on the airfoil surface the velocity was prescribed according to the stroke motion guarantying the no slip condition in the airfoil.

2.3 Membrane Equation

The dynamic of a moving web can be described by the thread-line model [Aidun and Qi (1998)].

$$m\frac{\partial^2 w}{\partial t^2}+2Vm\frac{\partial^2 w}{\partial x\partial t}+(V^2m-T)\frac{\partial^2 w}{\partial x^2}+D\frac{\partial^4 w}{\partial x^4}=p(x,t) \tag{3}$$

Where w is displacement in the thickness direction, t is time, m is the mass per unit area of the web, V the velocity of the web, T the tension of the web, D is the bending stiffness and $p(x,t)$ is the pressure in both top and bottom of the web.

If an inertial frame of reference is used, the variable V and the Coriolis force term can be neglected, thus equation (3) reduces to the typical web equation:

$$m\frac{\partial^2 w}{\partial t^2}-T\frac{\partial^2 w}{\partial x^2}+D\frac{\partial^4 w}{\partial x^4}=p(x,t) \tag{4}$$

In the case of a flexible membrane, in the limit of vanishing stiffness, the following assumption is valid:

$$T\left\|\frac{\partial^2 w}{\partial^2 x}\right\|\gg D\left\|\frac{\partial^4 w}{\partial x^4}\right\| \tag{5}$$

So that the equation (4) reduces to the well-known membrane equation without damping:

$$m\frac{\partial^2 w}{\partial t^2} - T\frac{\partial^2 w}{\partial x^2} = p(x,t) \tag{6}$$

The eigenvalues of equation (6) are real numbers, $\lambda_{1,2} = \pm\sqrt{\frac{T}{m}}$, denoting an hyperbolic differential equation. To solve this equation, we have to obtain the hydrodynamic force, $p(x,t)$, which couples membrane equation with the Navier-Stokes equations.

The Leap-Frog scheme computes the position and acceleration of each membrane element at each time instant and the velocity is computed at the average of each time-step. At the beginning, the acceleration is calculated from the equation (6) using second order finite difference scheme:

$$a(t) = \frac{p}{m} + \frac{T}{m\Delta x^2}(w_{i+1}^n - 2w_i^n + w_{i-1}^n) \tag{7}$$

Afterwards, the velocity is computed in the middle of the time step with the following equation:

$$v\left(t + \frac{\Delta t}{2}\right) = v\left(t - \frac{\Delta t}{2}\right) + \Delta t \times a(t) \tag{8}$$

and the position of the membrane can be computed in the new time instant:

$$w(t + \Delta t) = x(t) + \Delta t \times v\left(t + \frac{\Delta t}{2}\right) \tag{9}$$

After the position of the membrane is known, the time $t = t + \Delta t$ and the cycle starts again in equation (7). The conditional stability condition of the method requires that the time step:

$$\Delta t < \Delta x\sqrt{\frac{m}{T}} \tag{10}$$

To obtain the different resonance modes, we need to equal the frequency of the analytic solution with the flapping frequency, obtaining the following relation:

$$T = \frac{4f^2c^2m}{n^2} \tag{11}$$

The equation (11) allows to compute the tension which produces the desired n^{th} vibration mode, for a fixed membrane density m, for a flapping frequency f and c is the airfoil's chord.

The explicit temporal discretization for the membrane and the implicit solution of the fluid flow constitutes an accurate coupling algorithm because the inertia of the structure is very small. Otherwise, at each time step, the energy introduced by the fluid loading on the structure may create energy dissipation. If an implicit coupling is considered the coupling variables are exchanged and the fluid domain is updated at each time step. However for the present case, with very small displacements per time step the problem of energy conserving in the interface boundary is negligible.

3 Predictions for Rigid Airfoils

In this section, rigid airfoils with elliptic, plate or diamond shapes are calculated in the dragonfly mode with a stroke length A_0 and an angle of motion line β, see Fig. 2. The results of the elliptic airfoil were compared with reference published data [Wang (2000)].

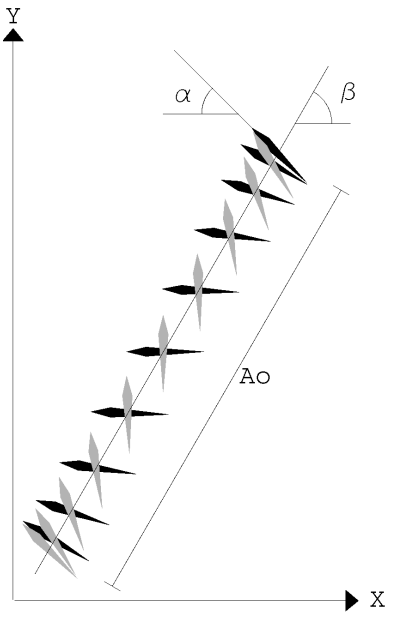

Figure 2: Dragonfly mode

Three levels of mesh refinement where considered corresponding to one, two and

four hundred thousand cells to discuss the solutions dependence on the mesh size. The time step corresponding to each mesh was selected, as $\Delta t = 0.02$ s, 0.01 s and 0.005 s, to guarantee the Courant number C corresponding to each mesh less than 0.5.

The dragonfly movement in hovering mode, used in the present work, is characterized by the translation and pitching motions given by the equations below [Wang (2000)]:

$$X(t) = \frac{A_0}{2} \cos\left(\frac{2\pi t}{P}\right) \tag{12}$$

$$\alpha(t) = \frac{\pi}{4}\left[1 - \sin\left(\frac{2\pi t}{P}\right)\right] \tag{13}$$

Where $X(t)$ is position of the airfoil center along the motion line, P is the stroke period, $\alpha(t)$ the pitch angle, A_0 the stroke length of 2,5 cm and $\beta = \pi/3$ is the angle of motion line.

The results were predicted as a benchmark test case, with an elliptic airfoil with 1 cm of chord and 1,25 mm of thickness. The maximum velocity of the airfoil, $U_{ref} = \pi$ corresponds to a Reynolds number equal to $Re = U_{ref}c/\upsilon = 157$. The kinematic viscosity (υ) is 2.0×10^{-4} m^2/s and the fluid density is 1.225 Kg/m^3. The rotation and translation Strouhal numbers are equal to $St_a = fA_0/U_{ref} = 0.318$ and $St_c = fc/U_{ref} = 0.127$, respectively. Twelve stroke cycles were predicted in each case to guarantee a periodic solution.

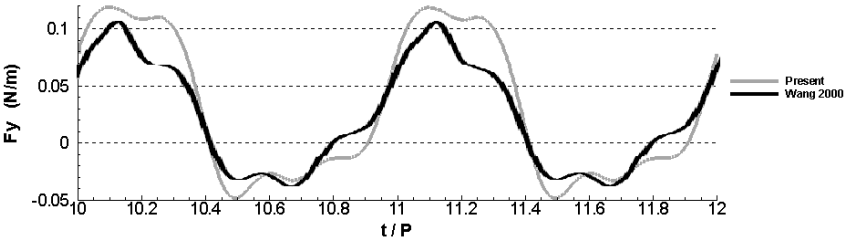

Figure 3: Lift force with the elliptic airfoil

Fig. 3 and Fig. 4 show the temporal evolution of the lift and drag forces, obtained with 400 thousands cells. The comparison with the reference results is globally in satisfactory agreement but some of the differences could be explained by the different numerical methods used and also by the different boundary conditions at far field. Wang uses 4^{th} order accurate numerical method but theoretically enforces the

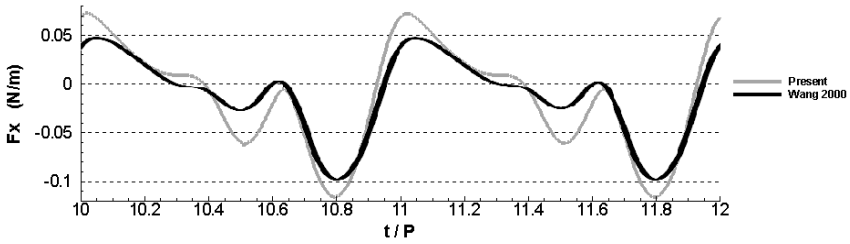

Figure 4: Drag force with elliptic airfoil

outer boundary condition, we use 2^{nd} order accuracy and the outer free boundary is located far away, but we use a very fine mesh comprising 400 thousands cells for a two-dimensional problem.

The average lift force component obtained during one cycle was predicted to be 2.96×10^{-2} N/m while Wang (2000) reported 2.8×10^{-2} N/m. Since the solution obtained with 400 thousand cells are in satisfactory agreement with the reference results and no differences were observed with the different mesh sizes, no further mesh refinement was considered.

Fig. 5 and Fig. 6 show the evolution of the lift and drag forces for $Re = 157$ and $Re = 1570$ with the elliptic airfoil. These figures help to understand the influence of the Reynolds number or the forces. The curves have a similar evolution but denote differences in the local relative extremes, these differences may be attributed to the occurrence of stronger vortices for $Re = 1570$ than for $Re = 157$.

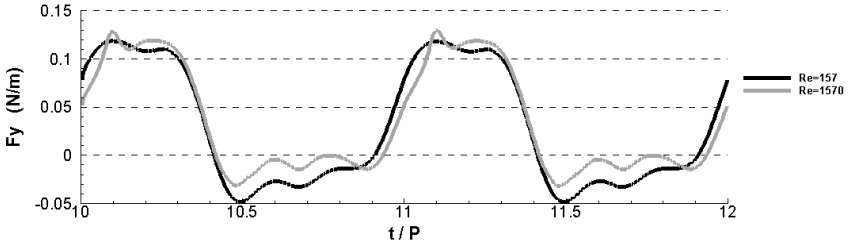

Figure 5: Lift force with elliptic airfoil for different Reynolds numbers

Fig. 7 and Fig. 8 compare the lift and drag forces for three rigid airfoils with elliptic, plate and diamond shapes, during the dragonfly mode at $Re = 157$. The lift and drag curves show a similar evolution for all the different shapes, but with some differences that can be analyzed in the contour plots of the vorticity field shown in Fig. 9. The plate and diamond, at point **A'**, marked in Fig. 7 and Fig. 8, display

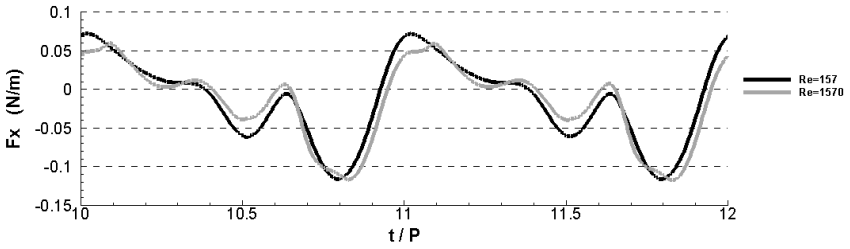

Figure 6: Drag force with elliptic airfoil for different Reynolds numbers

bigger vortices than the elliptic airfoil. Another difference appears in the leading edge vortex that makes the drag in the plate and diamond airfoils lower than for the elliptic airfoil, see Fig. 9. At point **D'**, the vortices attached to the airfoil are much more intense in the plate and diamond airfoils than in the elliptic one.

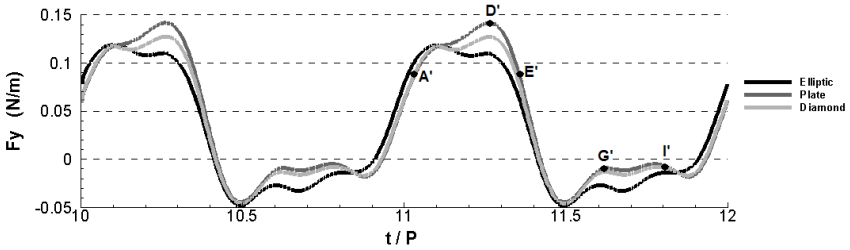

Figure 7: Lift force with the three rigid airfoils at $Re = 157$

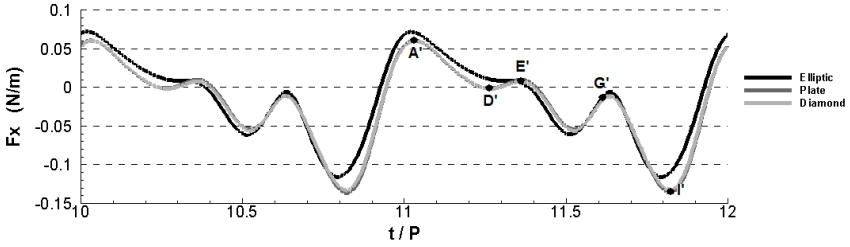

Figure 8: Drag force with the three rigid airfoils at $Re = 157$

Tab. 1 lists the average forces on each airfoil, the plate and diamond airfoils display similar drag and lift forces and the airfoils edges can explain the differences relatively to the elliptic airfoil. The sharp edges of the plate and diamond airfoils

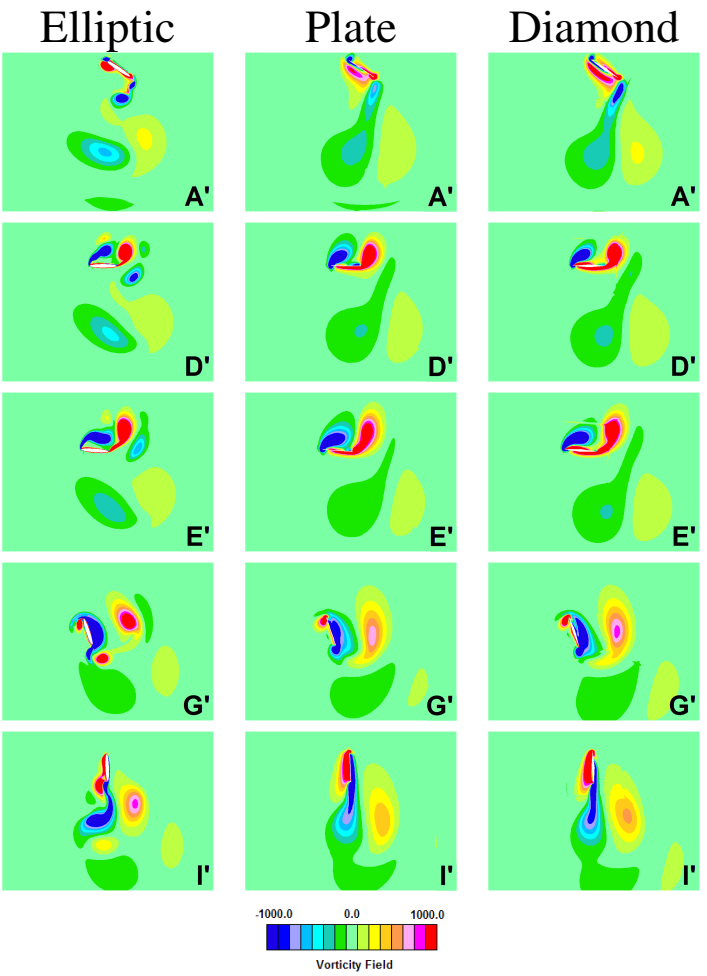

Figure 9: Vorticity field with the three rigid airfoils

generate a more intense LEV and a similar observation has been made by [Ansari, Knowles, and Zbikowski (2008)]. The airfoil shape is not a relevant design parameter compared with sharps leading and trailing edges, for the dragonfly hovering set of parameters studied.

Table 1: Average force values with the three rigid airfoils at $Re = 157$

Force (N/m)	**Elliptic**	**Plate**	**Diamond**
Lift	2.956×10^{-2}	3.659×10^{-2}	3.29×10^{-2}
Drag	-1.389×10^{-2}	-2.1088×10^{-2}	-2.094×10^{-2}

Fig. 10 shows the temporal evolution of the lift force for $Re = 1570$, the lift and drag forces evolution display similar differences for both Reynolds numbers. Tab. 2 lists the average forces values for each of the three airfoils investigated.

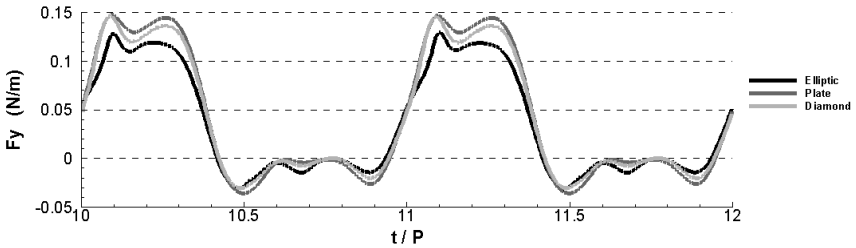

Figure 10: Lift force with the three rigid airfoils at $Re = 1570$

Table 2: Average force values with the three airfoils at $Re = 1570$

Force (N/m)	**Elliptic**	**Plate**	**Diamond**
Lift	3.484×10^{-2}	4.18×10^{-2}	4.08×10^{-2}
Drag	-1.633×10^{-2}	-2.111×10^{-2}	-1.979×10^{-2}

The diamond and plate airfoil coefficients are similar, which is an evidence of the edge shape contribution, over the airfoil thickness, to the vortices generation and their attachment to the airfoil, increasing the lift force.

4 Results for Flexible Membrane Airfoil

The prescription of the 1^{st}, 2^{nd} or 3^{rd} mode of vibration allows the calculation of the membrane tension via equation (11). The stroke length and oscillation period

was kept unchanged as well as the membrane density ($m = 2.0\,\mathrm{Kg/m^2}$). The membrane will flap in resonance mode and one expects that the membrane oscillation amplitude increases with time according to the viscous damping and the feedback mechanism. At $t = 0\,\mathrm{s}$ the initial membrane shape is geometrically flat and calculations were performed up to 20 stroke periods.

The membrane equation does not have damping terms and the membrane displacement will reach a periodic solution due to aerodynamic damping, which occurs in high frequency modes. Low frequencies should require a damping component in the structural model, since the goal is to study the resonance mode this term was not include.

4.1 First Mode of Vibration

The first mode of vibration was achieved with the prescription of $m = 2.0\,\mathrm{Kg/m^2}$ and $T = 1.28\,\mathrm{N/m}$. Fig. 11 and Fig. 12 show the evolution of the lift and drag forces with the rigid and flexible airfoils corresponding to the first mode of vibration.

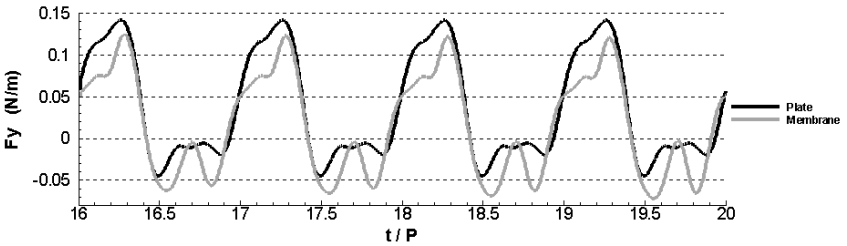

Figure 11: Lift force with the first mode of vibration

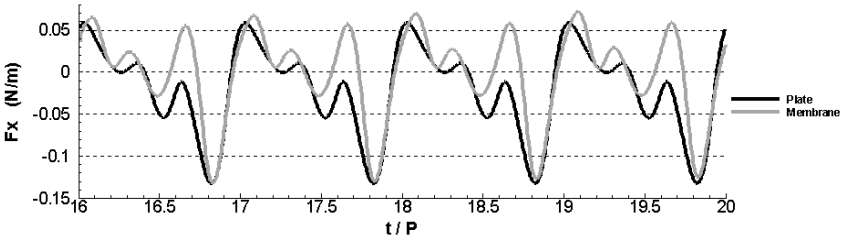

Figure 12: Drag force with the first mode of vibration

Fig. 13 shows the membrane displacement at three reference points of control $x = c/4$, $x = c/2$ and $x = 3c/4$ over four cycles of the simulation, where c is the airfoil chord and w the calculated membrane displacement.

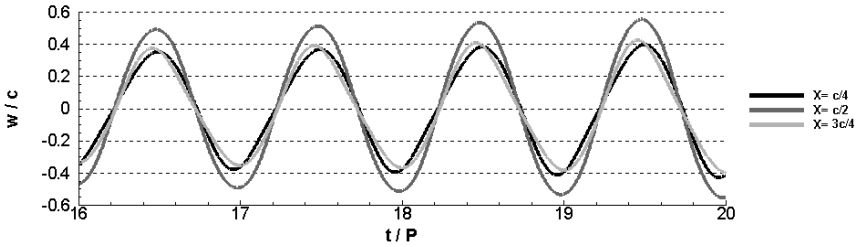

Figure 13: Membrane displacement with the first mode of vibration

The three curves have the same frequency, which is equal to the flapping frequency and the amplitude grows slightly as a consequence of the membrane being in resonance. The different curves are in phase, which is a characteristic of the first mode of vibration.

4.2 Second Mode of Vibration

The second mode of vibration was achieved prescribing $m = 2.0\,\mathrm{Kg/m^2}$ and $T = 0.32\,\mathrm{N/m}$. Fig. 14 and Fig. 15 show the evolution of the lift and drag forces corresponding to the membrane at the second mode of vibration and their comparison with the rigid plate airfoil case.

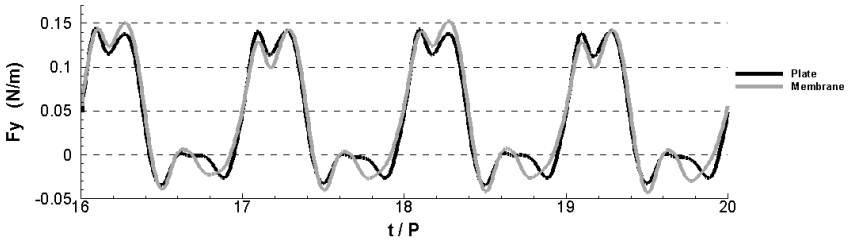

Figure 14: Lift force with the second mode of vibration

Fig. 16 shows the evolution of the membrane displacement, in the three reference points of control, during the last four cycles of the simulation. The curves of the points $x = c/4$ and $x = 3c/4$ are in opposite phase, which is a characteristic of the second mode of vibration. The evolution of the point corresponding to $x = c/2$ denotes a non periodical displacement from the nonlinear fluid structure interaction. During the twenty cycles of the simulation only a small amplification displacement is predicted. While the lift force shows periodicity every two cycles, the drag force is almost equal to the rigid flat plate values.

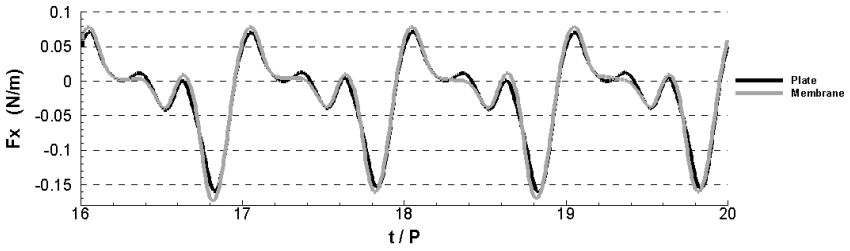

Figure 15: Drag force with the second mode of vibration

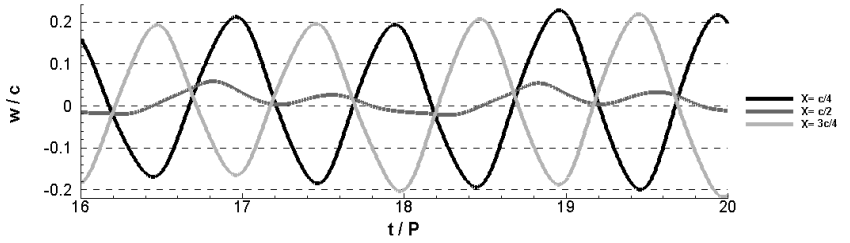

Figure 16: Membrane displacement with the second mode of vibration

4.3 Third Mode of Vibration

The third mode of vibration was achieved prescribing $m = 2.0\,\mathrm{Kg/m^2}$ and $T = 0.1422\,\mathrm{N/m}$. Fig. 17 and Fig. 18 show the evolution of the lift and drag forces for the flat plate and membrane airfoil at the third mode of vibration. Twenty cycles were not enough to reach a periodic solution. For this resonance mode the lift curve displays relatively large variations to the rigid plate counterpart.

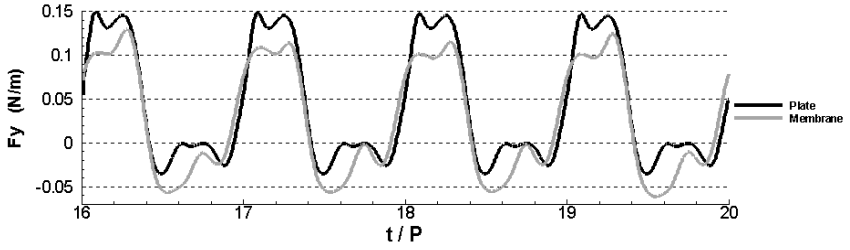

Figure 17: Lift force with the third mode of vibration

Fig. 19 shows the evolution of the membrane displacement in the three reference points of control, during the last four cycles of the simulation. The curves at points

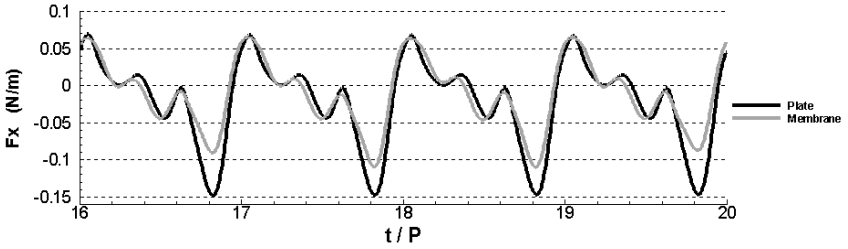

Figure 18: Drag force with the third mode of vibration

$x = c/4$ and $x = 3c/4$ are in phase while the point at $x = c/2$ is in opposite phase, which are characteristics of the third mode of vibration.

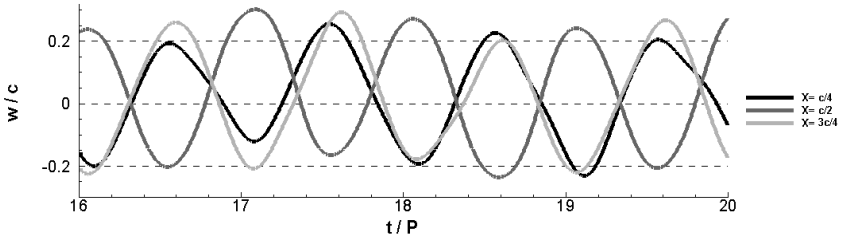

Figure 19: Membrane displacement with the third mode of vibration

4.4 Comparison of the resonance modes

Fig. 20 and Fig. 21 show the comparison of the lift and drag forces corresponding to the three resonance modes and the reference flat plate rigid case. The vorticity contours at each of the marked instants, during the last simulated cycle, are shown in Fig. 22 and a zoom is shown in Fig. 23.

Fig. 20 shows that at instant **A** lift drops at the 1^{st} and 3^{rd} mode cases, see also Fig. 22 and Fig. 23, these airfoils do not carry an attached vortex at the leading edge and the Kramer (rotational) effect explains the production of the lift force in the beginning of the downstroke, the same trend is observed for the temporal evolution of points **B** to **E**.

Fig. 21 shows the drag force evolution denoting smaller differences than the ones observed for the lift force and occur mainly at points **F** and **H**. Point **F** denotes an increase in the drag force for the 1^{st} mode at the beginning of the upstroke (point **E**) corresponding to the membrane maximum displacement at point **F**. The membrane

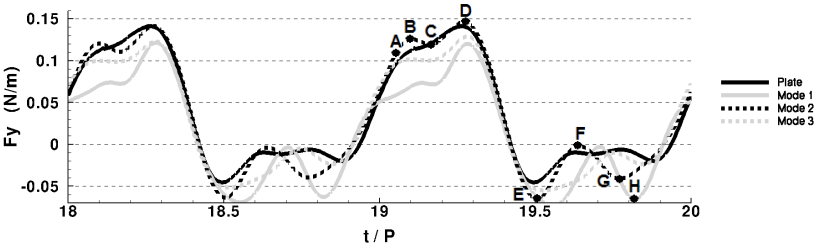

Figure 20: Lift force with the plate and membrane airfoils

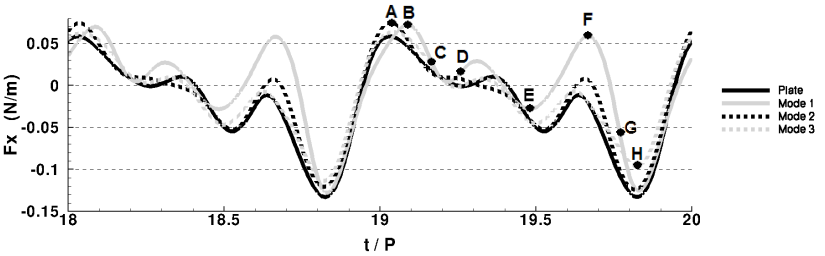

Figure 21: Drag force with the plate and membrane airfoils

movement will push the fluid to the opposite side of the airfoil's movement increasing the drag force. The 3^{rd} mode promotes a high drag force at point **H**, since the two displacement peaks of the membrane will push the fluid in the opposite direction of the movement, which can been seen at point **F**, plus the detachment of the leading edge vortex at point **H**.

Tab. 3 lists the average value of the lift and drag forces calculated during the 20^{th} stroke. The positive lift force drop and the drag value corresponding to the 1^{st} resonance mode airfoil, are a consequence of the drag peak observed at point **F**, the signal of the average force in the x axis is reverted. In addition the lift over drag ratio is higher in the vibration modes than for the rigid flat plate.

Table 3: Values of Lift and Drag forces with the plate and membrane airfoils

Force (N/m)	**Plate**	1^{st} **Mode**	2^{nd} **Mode**	3^{rd} **Mode**
Lift	3.659×10^{-2}	1.398×10^{-2}	3.472×10^{-2}	2.766×10^{-2}
Drag	-2.109×10^{-2}	1.184×10^{-3}	-1.469×10^{-2}	-1.112×10^{-2}
Lift / Drag	-1.735	11.807	-2.384	-2.487
Lift / Lift rigid	1.0	0.382	0.924	0.7558

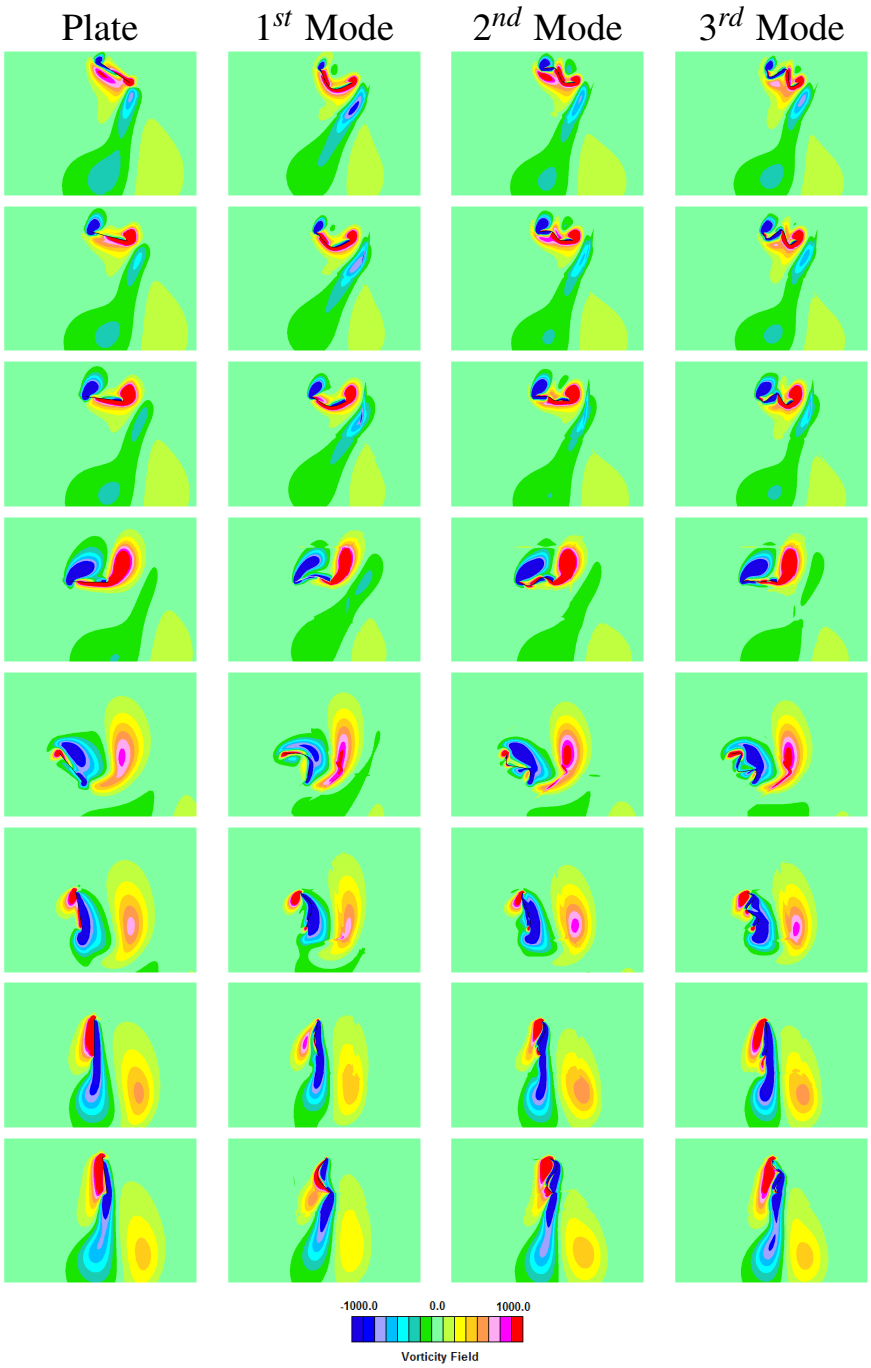

Figure 22: Vorticity field with the plate and membrane airfoils (**A** to **H**, see Fig. 20)

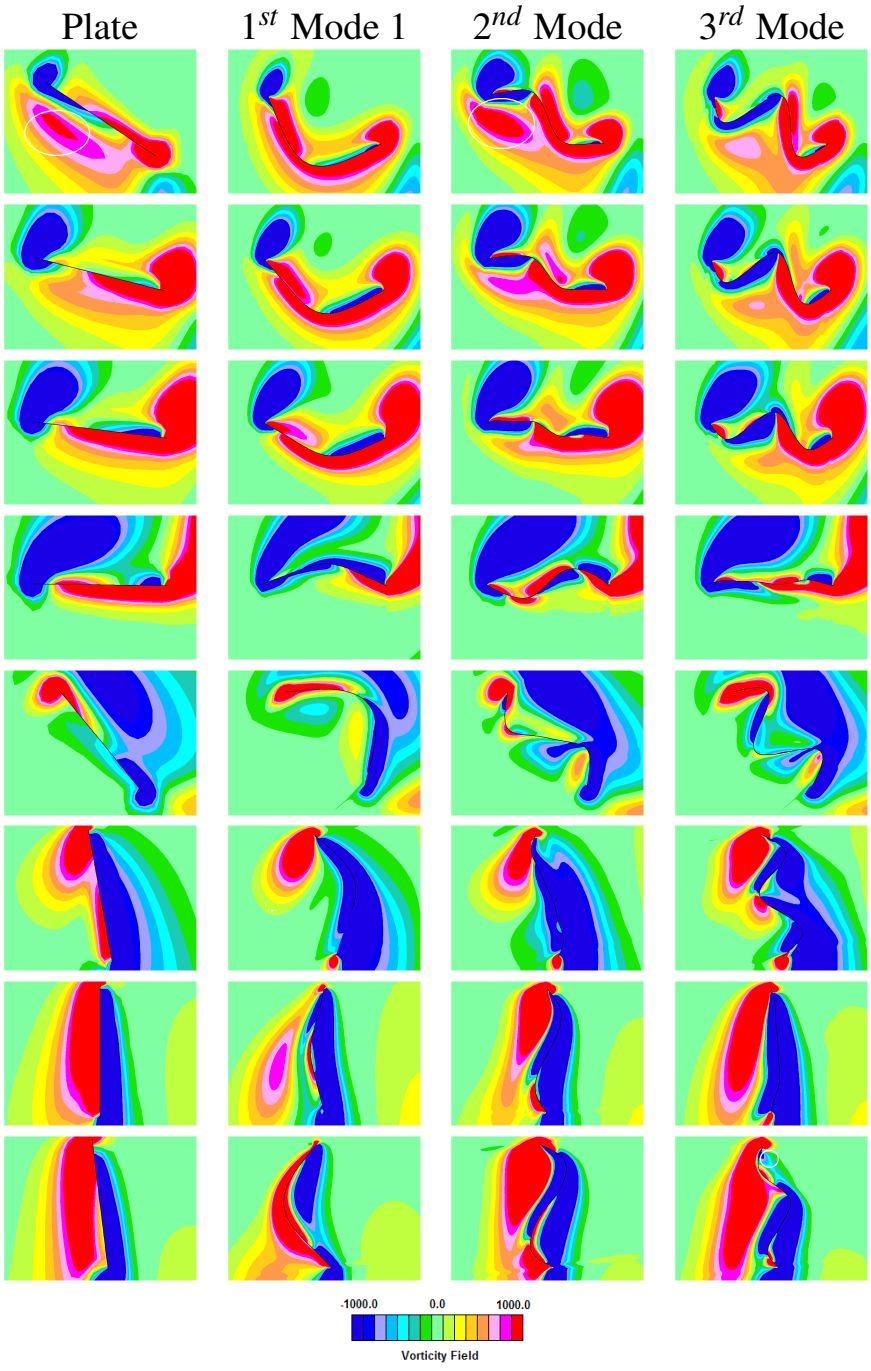

Figure 23: Vorticity field with the plate and membrane airfoils detailed

The expected difficult problem of membrane displacement prediction due to aeroelasticity fluid structure coupling was not found despite off the extreme cases of flapping resonance modes investigated. Rather, the computed instantaneous spatial airfoil bending, in turn, may be inserted on a computational fluid model, without the need for the full fluid-membrane interaction.

4.5 Energy Balance

The section presents the calculations of the power required during dragonfly mode, taking into account only the aerodynamic forces. The inertial forces were not accounted for because the rigid and the resonant airfoils have the same mass distribution and, consequently, the power required due to inertial forces is the same. Our goal is to compare the differences in the energy consumption among the four airfoils.

The energy balance can be divided in three contributions. The power required for the pitching motion is denoted by C_pR and the power required for the translation motion in the x and y axis is denoted by C_pT_x and C_pT_y, respectively.

$$C_pR = \frac{-\alpha'(t)M_R}{0.5\rho U_{ref}^3 S} \tag{14}$$

$$C_pT_y = \frac{F_y \sin(\beta)X'(t)}{0.5\rho U_{ref}^3 S} \tag{15}$$

$$C_pT_x = \frac{F_x \cos(\beta)X'(t)}{0.5\rho U_{ref}^3 S} \tag{16}$$

Where ρ is the fluid density, U_{ref} is the reference velocity, S is the wing area, F_x and F_y are both the forces in the x and y axis and β is the angle of motion line, $X'(t)$, is the velocity along the motion line, $\alpha'(t)$ is the pitch velocity and M_R is the pitching moment, the pitch angle is positive in the clockwise direction.

4.5.1 Rigid Plate Analysis

The Fig. 24 shows the evolution of three power coefficients and the total coefficient for the rigid airfoil. The C_pT_y coefficient denotes that the downstroke is dominated by a large power coefficient value which is caused by the airfoil high angle of attack. At the end of each stroke, there is a small time interval with negative values that explain the amplitude limitation, identified by (Sun and Tian (2002)).

The C_pT_x coefficient presents, at the begin of the upstroke, two peaks due to the vortex presence and removal on the airfoil upper surface. The oscillations are caused by changes of the angular velocity and the angle of attack of the airfoil, during the downstroke.

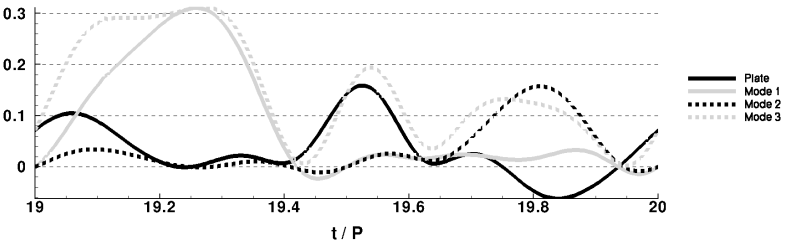

Figure 24: Potency coefficients with the plate airfoil

4.5.2 Rigid and Flexible Airfoils Comparison

During the beginning of the upstroke Fig. 25 shows that the (C_pR) pitch potency coefficient corresponding to the 1^{st} mode of vibration displays the lowest negative values because membrane motion is in opposite direction of the airfoil motion. In the literature, the negative work contribution has received several interpretations being the one given by Weis-Fogh (1972) attributed to an elastic element that could extract energy and release it later.

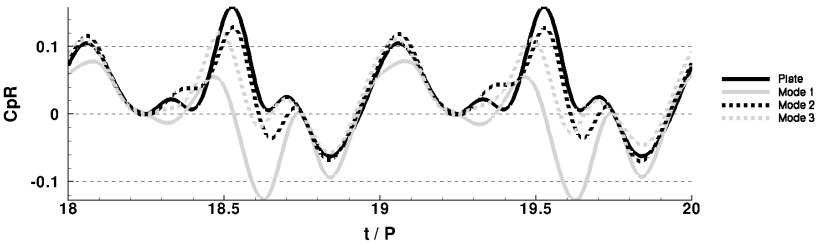

Figure 25: Pitch potency coefficient with the plate and membrane airfoils

Fig. 26 shows the lift potency coefficient evolution. During the downstroke, the 1^{st} mode displays slightly lower values, according to the observed in the lift force. During the upstroke, the airfoil is moving upwards and the C_pT_y is positive. The resonant airfoils exhibit higher C_pT_y because they have higher lift absolute values than the rigid airfoil.

The drag potency coefficient evolution, shown in Fig. 27, follows the drag force already seen in Fig. 21. The drag peak, at point **F** of the 1^{st} mode of vibration, results in a local minimum in the C_pT_x evolution which has a negative value since the membrane movement contradicts the airfoil motion.

The C_pTotal evolution shown in Fig. 28 attributes the lowest absolute value to the

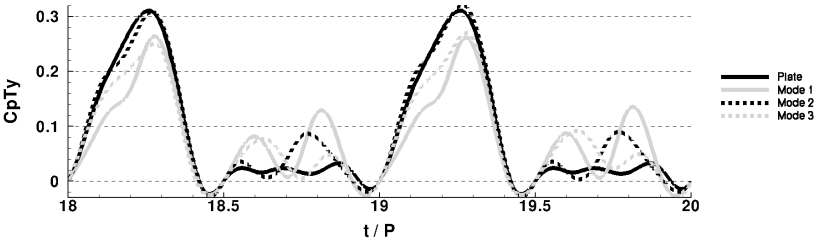

Figure 26: Lift potency coefficient with the plate and membrane airfoils

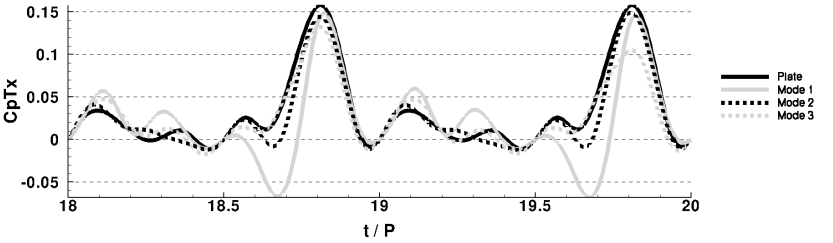

Figure 27: Drag potency coefficient with the plate and membrane airfoils

1^{st} mode. Although there is a significant reduction in the energy consumption in the 1^{st} mode, the lift loss is higher than in the other airfoils studied. Some extra energy is required, during the downstroke, due to the membrane upward movement (relative to its reference). During the upstroke, the membrane downward movement contradicts the airfoil movement creating a positive effect in the drag force and consequently in the C_pT_x.

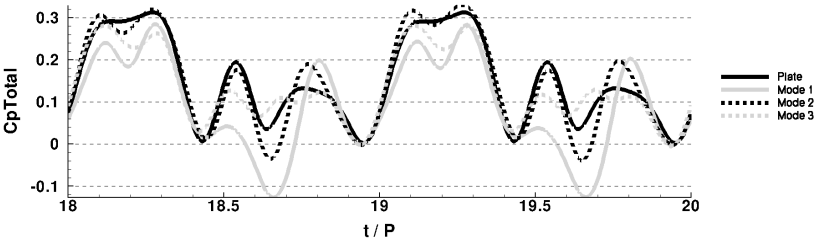

Figure 28: Total potency coefficient with the plate and membrane airfoils

Tab. 4 shows the work done during the 20^{th} stroke and obtained by integration of the power coefficient over time. Tab. 5 lists the work done taking into account only the positive work.

Table 4: Average values of work coefficients with the plate and membrane airfoils

Power	**Plate**	$1^{s}t$ **Mode**	2^{nd} **Mode**	3^{rd}**Mode**
CwR	3.282×10^{-2}	-5.925×10^{-3}	2.881×10^{-2}	2.931×10^{-2}
CwTy	8.384×10^{-2}	7.283×10^{-2}	9.15×10^{-2}	7.901×10^{-2}
CwTx	3.387×10^{-2}	2.508×10^{-2}	2.765×10^{-2}	2.704×10^{-2}
CwTotal	1.505×10^{-1}	9.288×10^{-2}	1.48×10^{-1}	1.354×10^{-1}
CwTotal relative	1.0	0.617	0.983	0.9
Lift / CwTotal	0.243	0.151	0.236	0.204

Table 5: Average values of positive work coefficients for plate and membrane airfoils

Power	**Plate**	1^{st} **Mode**	2^{nd} **Mode**	3^{rd} **Mode**
CwR	4.015×10^{-2}	1.962×10^{-2}	3.834×10^{-2}	3.575×10^{-2}
CwTy	8.564×10^{-2}	8.107×10^{-2}	9.407×10^{-2}	8.222×10^{-2}
CwTx	3.484×10^{-2}	2.823×10^{-2}	2.958×10^{-2}	2.896×10^{-2}
CwTotal	1.505×10^{-1}	1.053×10^{-1}	1.495×10^{-1}	1.354×10^{-1}
CwTotal relative	1.0	0.7	0.993	0.9
Lift / CwTotal	0.243	0.133	0.232	0.204

The CpR values for the resonant airfoils 2^{nd} and 3^{rd} modes differ tipically 10 to 20% of the analog results for the rigid flat plate airfoil. The first mode displays values above 50%. The energetic analysis support the flow dynamics related with the very small contribution of airfoil shape for hovering flight.

5 Conclusions

Predictions of 2D airfoils in hovering flight were presented for rigid and for flexible resonant membranes. The computational procedure and methodology was validated with a variety of benchmark tests of a rigid airfoil in hovering flight and the results show satisfactory agreement with the instantaneous drag and lift forces reported by Wang [Wang (2000)]. The following conclusions could be withdrawn.

- Three rigid airfoil shapes in hovering flight were compared, flat plate, elliptical and diamond, at $Re = 157$ and $Re = 1570$. The predicted near and far field vortical structures are very similar for the different airfoil shapes because the leading and trailing edge vortices are almost independent on the 2D airfoil curvature. The predicted forces noticeable differences are attributed to the edge curvature angle of the airfoil shapes. The profiles with sharp edges,

flat plate and diamond shape, promote strong LEV and contrary, the round leading edge of the elliptical profile shape decreases the LEV intensity and reduces the vortices residence time over the airfoil.

- Once validated the numerical tool for flapping airfoils, we have considered a flexible flat-plate airfoil in dragonfly hovering and in resonant mode. The flapping frequency was made equal to the natural frequency of the 1D membrane, being the number frequency mode inversely proportional to the tension. Although the membrane is highly deformed the predicted drag and lift forces are very much similar to the flat-plate results despite of a highly deformed membrane, during the second or third resonant modes, the drag and lift forces. The inertial and elastic components do not dominate the system behavior in these operation modes. The membrane bending, associated with the first mode strongly minimizes the drag force but the lift decreases due to drag role in dragonfly mode, consequently the lift over drag coefficient increases substantially.

- The energy global balance and the instantaneous power coefficients during the 2^{nd} and 3^{rd} vibration modes are withing 20% of the values predicted to the rigid airfoil despite of the differences presented in the airfoil shapes. The first vibration mode differs substancialy due to the membrane shape motion relatively to the surrounding flow.

- The results obtained in this study provide physical insight into the understanding of unsteady aerodynamics and flow structures during 2D inclined hovering flight. The results shed some light to study in detail the modes of vibration on membrane oscillations. Future studies may be concerned with stiffness that may create different vibration modes resulting on unsteady interactions with the wake.

Acknowledgement: The first author gratefully acknowledge the support received by the Portuguese FCT (Foundation for Science and Technology) Grant SFRH/BD/48150/2008.

References

Aidun, C. K.; Qi, D. W. (1998): A new method for analysis of the fluid interaction with a deformable membrane. *The Journal of Statistical Physics, Vol. 90, pp. 145-158.*

Andro, J. Y.; Jacquin, L. (2009): Frequency effects on the aerodynamic mechanisms of a heaving airfoil in a forward flight configuration. *Aerospace Science and Technology, Vol. 13, pp. 71-80*.

Ansari, S. A.; Knowles, K.; Zbikowski, R. (2008): Insectlike flapping wings in the hover part 2: Effect of wing geometry. *Journal of Aircraft, Vol. 45, 6, pp. 1976-1990*.

Ansari, S. A.; Zbikowski, R.; Knowles, K. (2006): Aerodynamic modelling of insect-like flapping flight for micro air vehicles. *Progress in Aerospace Sciences, Vol. 42, pp. 129-172*.

Birch, J. M.; Dickinson, M. H. (2001): Spanwise flow and the attachment of the leading-edge vortex on insect wings. *Nature, vol. 412, n. 6848, pp. 729-733*.

Bisplinghoff, R. L.; Ashley, H.; Halfman, H. (1996): *Aeroelasticity*. Dover Science.

Combes, S. A.; Daniel, T. L. (2001): Shape, flapping and flexion: Wing and fin design for forward flight. *The Journal of Experimental Biology, Vol. 204, pp. 2073-2085*.

Daniel, T.; Combes, S. (2001): Flexing wings and fins: bending by inertial or fluid dynamic forces. *Int. Comp Biol, Vol. 42, pp. 1044-1049*.

Dickinson, M. H.; Götz, K. G. (1993): Unsteady aerodynamic performance of model wings at low reynolds numbers. *The Journal of Experimental Biology, Vol. 174, pp. 45-64*.

Dickinson, M. H.; Lehmann, F. O.; Sane, S. P. (1999): Wing rotation and the aerodynamic basis of insect flight. *Science, Vol. 284, pp. 1954-1960.*

Dudley, R. (2000): *The biomechanics of insect flight form, function, evolution*. Princeton Press , Princeton, New Jersey.

Eldredge, J. D. (2005): Efficient tools for the simulation of flapping wing flows. *43rd AIAA Aerospace Sciences Meeting and Exhibit, Reno, Nevada, U.S.A., 10-13 January*.

Ellington, C. P. (1984): The aerodynamics of hovering insect flight iv. aerodynamic mechanisms. *Philos. Trans. R. Soc. London, Ser. B 305*.

Ellington, C. P. (1999): The novel aerodynamics of insect flight: applications to micro-air vehicles. *The Journal of Experimental Biology, Vol. 202, pp. 3439-3448*.

Ellington, C. P.; Berg, C. V. D.; Willmott, A. P.; Thomas, A. L. R. (1996): Leading-edge vortices in insect flight. *Nature, Vol. 384, pp.626-630*.

Galvao, R.; Israeli, E.; Song, A.; Tian, X.; K., B.; Sharon, S.; B., K. (2006): The aerodynamics of compliant membrane wings modeled on mammalian flight mechanics. *In Proceedings 36th AIAA Fluid Dynamics Conference and Exhibit,5 - 8 June 2006, San Francisco, California*.

Gao, T.; Lu, X. (2008): Insect normal hovering flight in ground effect. *Physics of Fluids, 20, 087101*.

Greenewalt, C. H. (1960): The wings of insects and birds as mechanical oscillators. *Proc. Amer. Phil. Soc., Vol. 104, pp. 605-611*.

Heathcote, S.; Wang, Z.; Gursul, I. (2008): Effect of spanwise flexibility on flapping wing propulsion. *Journal of Fluid and Structures, Vol. 24, pp. 183-199*.

Ho, S.; Nassef, H.; Pornsinsirirak, N.; Tai, Y. C.; Ho, C. M. (2003): Unsteady aerodynamics and flow control for flapping wing flyers. *Progress in Aerospace Sciences, Vol. 39, Issue 8, pp. 635-681*.

Hu, H.; Tamai, M.; Murphy, J. T. (2008): Flexible-membrane airfoils at low reynolds numbers. *Journal of Aircraft, Vol. 45, 5, pp. 1767-1778*.

Isogai, K.; Kamisawa, Y.; Sato, H. (2007): Resonance type flapping wing for a micro air vehicle. *AIAA Atmospheric Flight Mechanics Conference and Exhibit 20-30 August , South Carolina*.

Issa, R. (1985): Solution of the implicity discretised fluid flow equations by operator-splitting. *J. Comput. Phys., Vol. 62, 1, pp. 40-65*.

Kamakoti, R.; Lian Y.; Regisford, S. K. A.; Shyy, W. (2002): Computational aeroelasticity using a pressure-based solver. *CMES: Computer Modeling in Engineering and Science, Vol. 3, 6, pp. 773-790*.

La Mantia, M.; Dabnichki, P. (2008): Unsteady 3d boundary element method for oscillating wing. *CMES: Computer Modeling in Engineering and Science, Vol. 33, 2, pp. 131-153*.

Lehmann, F. O.; Dickinson, M. H. (1997): The changes in power requirements and muscle efficiency during elevated force production in the fruitfly drosophila melanogaster. *The Journal of Experimental Biology, Vol. 200, pp. 1133-1143*.

Lehmann, F. O.; Sane, S. P.; Dickinson, M. H. (2005): The aerodynamic effects of wingwing interaction in flapping insect wings. *The Journal of Experimental Biology, Vol. 208, pp. 3075-3092*.

Levin, O.; Shyy, W. (2001): Optimization of a low reynolds numbers airfoil with flexible membrane. *CMES: Computer Modeling in Engineering and Science, Vol. 2, 4, pp. 523-536*.

Lisa, A. M.; Deborah, M. G.; Chris, J. K. (2008): Numerical simulation of viscous flow interaction with an elastic membrane. *International Journal for Numerical Methods in Fluids, Vol. 57, pp. 1577-1602*.

Liu, H. (2009): Integrated modeling of insect flight: from morphology, kinematics to aerodynamics. *Journal of Computational Physics, Vol. 228, pp. 439-459*.

Liu, H.; Ellington, C. P.; Kawachi, K.; Van den Berg, C.; Willmott, A. P. (1998): A computational fluid dynamic study of hawkmoth hovering. *The Journal of Experimental Biology, Vol. 201, pp. 461-477*.

Michelson, R. C.; Naqvi, M. A. (2003): Beyond biologically-inspired insect flight. *von Karman Institute for Fluid Dynamics RTO/AVT Lecture Series on Low Reynolds Number Aerodynamics on Aircraft Including Applications in Emerging UAV Technology, Brussels Belgium, 24-28 November*.

Pereira, J. M. C.; Maia, N. A. R.; Pereira, J. C. F. (2009): A computational fluid dynamics study of a 2d airfoil in hovering flight under ground effect. *CMES: Computer Modeling in Engineering and Science, Vol. 49, No. 2, pp. 113-141*.

Ramamurti, R.; Sandberg, W. C. (2002): A three-dimensional computational study of the aerodynamic mechanisms of insect flight. *The Journal of Experimental Biology, Vol. 205, pp. 1507-1518*.

Rojratsirikul, P.; Wang, Z.; Gursul, I. (2009): Unsteady fluid-structure interactions of membrane airfoils at low reynolds numbers. *Experiments in Fluids, Vol. 46, 5, pp. 859-872*.

Rozhdestvensky, K. V.; Ryzhov, V. A. (2003): Aerohydrodynamics of flapping wing propulsors. *Progress in Aerospace Sciences, Vol. 39, pp. 585-633*.

Sane, S. P. (2003): The aerodynamics of insect flight review. *The Journal of Experimental Biology, Vol. 206, pp. 4191-4208*.

Shyy, W.; Berg, M.; Ljungqvist, D. (1999): Flapping and flexible wings for biological and micro vehicles. *Progress in Aerospace Sciences, Vol. 35, 5, pp. 455-506*.

Shyy, W.; Jenkins, D. A.; Smith, R. W. (1997): Study of adaptive shape airfoils at low reynolds number in oscillatory flow. *AIAA Journal, Vol. 35, pp. 1545-1548*.

Shyy, W.; Lian, Y.; Tang, J.; Viieru, D.; Liu, H. (2008): *Aerodynamics of Low Reynolds Number Flyers*. Cambridge University Press.

Smith, R.; Shyy, W. (1995): Computation of unsteady laminar flow over a flexible two-dimensional membrane wing. *Physics of Fluids, Vol. 7, 9, pp. 2175-2184*.

Srinath, D. N.; Mittal, S.; Manek, V. (2009): Multi-point shape optimization of airfoils at low reynolds numbers. *CMES: Computer Modeling in Engineering and Science, Vol. 51, 2, pp. 169-190*.

Sun, M.; Tian, J. (2002): Lift and power requirements of hovering flight in drosophila virilis. *The Journal of Experimental Biology, Vol. 205, pp. 2413-2427*.

Thomas, A. L. R.; Taylor, G. K.; Srygley, R. B.; Nudds, R. L.; Bomphrey, R. J. (2002): Dragonfly flight: free-flight and tethered flow visualizations reveal a diverse array of unsteady lift-generating mechanisms, controlled primarily via angle of attack. *The Journal of Experimental Biology, Vol. 207, pp. 4299-4323*.

Thomas, L. D.; Stancey, A. C. (2002): Flexible wings and fins: Bending by inertial or fluid-dynamic forces. *Integrative and Comparative Biology, Vol. 42, pp. 1044-1049*.

Van den Berg, C.; Ellington, C. P. (1997): The vortex wake of a 'hovering' model hawkmoth. *Phil. Trans. R. Soc. Lond. B, 352, pp. 317-328*.

Vanella, M.; Fitzgerald, T.; Preidikman, S.; Balaras, E.; Balachandran, B. (2009): Influence of flexibility on the aerodynamic performance of a hovering wing. *The Journal of Experimental Biology, Vol. 212, pp. 95-105*.

Wang, J.; Birch, J. M.; Dickinson, M. H. (2004): Unsteady forces and flows in low reynolds number hovering flight: two-dimensional computations vs robotic wing experiments. *The Journal of Experimental Biology, Vol. 207, pp. 449-460*.

Wang, J. Z. (2004): The role of drag in insect hovering. *The Journal of Experimental Biology, Vol. 207, pp. 4147-4155*.

Wang, Z. J. (2000): Two dimensional mechanism for insect hovering. *Physical Review Letters, Vol. 85, n. 10, pp. 2216-2219*.

Wang, Z. J. (2005): Dissecting insect flight. *Annu. Rev. Fluid Mech, Vol. 37, pp. 183-210*.

Weis-Fogh, T. (1972): Energetics of hovering flight in hummingbirds and in *Drosophila*. *The Journal of Experimental Biology, Vol. 59, pp. 169-230*.

Yamada, T.; Yoshimura, S. (2008): Line search partitioned approach for fluid-structure interaction analysis of flapping wing. *CMES: Computer Modeling in Engineering and Science, Vol. 24, 1, pp. 51-60*.

Young, J.; Lai, J. C. S.; Germain, C. (2008): Simulation and parameter variation of flapping-wing motion based on dragonfly hovering. *AIAA Journal, Vol. 46, 4, pp. 918-924*.